Title	Energy response of a passive variable friction damper and numerical simulation on the control effects for high-rise buildings
Author(s)	Shirai, Kazutaka; Sano, Takeshi; Suzui, Yasumasa
Citation	Structural Control and Health Monitoring, 29(12), e3124 https://doi.org/10.1002/stc.3124
Issue Date	2022-12
Doc URL	http://hdl.handle.net/2115/90707
Rights	This is the peer reviewed version of the following article: Shirai, K, Sano, T, Suzui, Y. Energy response of a passive variable friction damper and numerical simulation on the control effects for high-rise buildings. Struct Control Health Monit. 2022; 29(12):e3124, which has been published in final form at https://doi.org/10.1002/stc.3124. This article may be used for non-commercial purposes in accordance with Wiley Terms and Conditions for Use of Self-Archived Versions. This article may not be enhanced, enriched or otherwise transformed into a derivative work, without express permission from Wiley or by statutory rights under applicable legislation. Copyright notices must not be removed, obscured or modified. The article must be linked to Wiley ’ s version of record on Wiley Online Library and any embedding, framing or otherwise making available the article or pages thereof by third parties from platforms, services and websites other than Wiley Online Library must be prohibited.
Type	article (author version)
File Information	SCHM_MainText_r06b.pdf

Energy response of a passive variable friction damper and numerical simulation on the control effects for high-rise buildings

Kazutaka SHIRAI [1], Takeshi SANO [2], Yasumasa SUZUI [3]

[1] Faculty of Engineering, Hokkaido University, Japan. shirai.kazutaka@eng.hokudai.ac.jp
[2] Technology Division, Obayashi Corporation, Japan. sano.takeshi@obayashi.co.jp
[3] Technology Research Institute, Obayashi Corporation, Japan. suzui.yasumasa@obayashi.co.jp
Corresponding author: [1] Kazutaka SHIRAI
ORCID: [1] Kazutaka SHIRAI: 0000-0001-8712-9779

Abstract

In this study, the behavior of a passive displacement-dependent variable friction damper (VFD) was evaluated. The energy response behavior of a VFD specimen was investigated by conducting full-scale dynamic loading tests. Full-scale tests demonstrated that the VFD specimen produced a lower sliding force when the device response exceeded a predetermined displacement, resulting in a decreased dissipated energy ratio as the displacement increased. The VFD specimen exhibited stable energy response behavior as well as a stable friction sliding force and friction coefficient under sinusoidal, seismic response, and 100-cycle loadings. The energy response of the VFD specimen was almost independent of the loading frequency. Moreover, a response simulation was conducted using a two-dimensional 30-story nonlinear mainframe model with brace-type VFDs under various input motions, including observation records and long-period, long-duration waves. From the numerical simulations, the peak story drift in the case with brace-type VFDs was not significantly greater than in the case with conventional friction dampers (FDs). The dissipated energy ratios of the mainframe and dampers in the case with the VFDs were approximately identical to those in the case with the FDs. In comparison with conventional FDs, VFDs can produce a lower peak story shear force and axial compressive force in the lowest-story columns at the device installation span.

Keywords

Friction damper; energy response; long-period, long-duration ground motion; passive variable damper; variable friction damper; high-rise building

1 Introduction

In recent decades, friction devices have been used to control structures’ responses to dynamic disturbances such as earthquakes. In addition to their energy dissipation capabilities, friction dampers can provide a high initial stiffness compared with other types of damping devices. To date, many friction devices have been proposed, developed, and studied. These friction dampers can be sorted into three categories: (1) passive friction dampers with the aim of exerting an approximately constant sliding force; (2) active or semi-active variable friction dampers and control systems; and (3) passive variable friction dampers whose characteristics, such as the sliding force, can be varied intentionally.

Various research has been conducted on passive friction devices of category (1) and their response control effects[1–15]. However, this type of friction device cannot alter the sliding force during an earthquake and thus may introduce challenges in dealing with advanced structural vibration control problems that require the friction force to vary with the device displacement. As for category (2), active and semi-active variable friction devices and control systems have been studied both experimentally and numerically[16–28]. Many of these studies have used or assumed a variable device sliding force, mainly by controlling the crimping force on frictional surface using hydraulic, pneumatic, electromechanical, electromagnetic, and piezoelectric actuators. However, because active and semi-active control systems generally require external electric power, their reliability for extremely rare events, such as severe earthquakes, may be relatively low in comparison with that of passive systems.

Regarding category (3), several passive variable friction devices have been proposed. Roik et al. reported a three-stage frictional grip device[29]. FitzGerald et al. studied slotted bolted connections (SBCs) with two-state friction forces[30]. The SBCs exhibit rectangular hysteretic loops with a relatively small friction force within the predetermined displacement range and a relatively large friction force beyond this predetermined range. Nims et al. reported an energy-dissipating restraint with self-centering characteristics, the core of which consists of wedges and a spring[31]. Passive devices that exhibit flag-shaped hysteretic loops have also been studied in past work[32–34], as well as one with origin-oriented triangular hysteretic loops using a wedge-form part to change the friction force depending on the damper displacement[35]. Regarding sliding isolators for seismic isolation, a variable curvature friction pendulum system with a softening restoring force mechanism by a non-spherical sliding surface was studied[36,37]. Panchal and Jangid investigated a variable frictional coefficient pendulum device produced by gradually varying the roughness of a spherical surface[38]. Wang et al. experimentally investigated an arc-surfaced frictional device that yields an increased sliding force as the device displacement increases[39]. Downey et al. experimentally studied a cam-based passive variable frictional device that produces a decreased or increased sliding force as the device displacement increases using prototype elemental specimens[40]. Barzegar et al. numerically evaluated the response of multi-story building structures incorporating the cam-based device producing a decreased sliding force subjected to wind loads[41]. They also numerically investigated the response of structures incorporating the cam-based device with an increased sliding force under seismic excitations[41]. Zhao et al. experimentally studied a response-amplified frictional device, which comprises an inerter device and a gap element[42].

The present authors have previously proposed a passive variable friction damper (VFD) and conducted full-scale loading tests to grasp its basic characteristics[43,44]. Unlike the abovementioned friction devices in categories (1)–(3), the proposed VFD passively yields a reduced friction sliding force when the device response exceeds a predetermined displacement. Also, the authors have carried out numerical response simulations using high-rise steel frame building models with VFDs[45–48]. It is expected that this passive displacement-dependent ability of the sliding force of the VFD may be especially suitable for the aseismic retrofitting of existing high-rise buildings to withstand strong earthquakes, including long-period, long-duration (LPLD) waves.

However, to the best of the authors' knowledge, no past studies have investigated and clarified the energy response behavior of passive variable friction devices, including the VFD considered in the present study, that produce a decreased sliding force as the device displacement increases based on full-scale dynamic loading experiments and numerical simulations of nonlinear building mainframe structures subjected to various seismic motions. Therefore, the energy response behavior of the VFD has not yet been clarified. Moreover, the nonlinear response behavior of high-rise buildings with VFDs under various input motions, including observed records and LPLD ground motions, remains unclear.

The aim of the present study was to evaluate the energy response behavior of the VFD based on experimental results of full-scale dynamic loadings. Furthermore, to assess the seismic control effects produced by the VFD in a high-rise building, a numerical response analysis was carried out using a nonlinear frame structure model with installed VFDs under various input motions, including motions based on observation records and LPLD ground motions. This study contributes to the effective design of passive variable friction devices in consideration of the energy dissipation effects to enhance the response control performance for high-rise building structures against strong earthquakes such as LPLD ground motions.

2 Variable Friction Damper

The main feature distinguishing the VFD from a conventional friction damper (FD) is explained in this section. The VFD is an advanced device in which passive variable friction force characteristics are added to an FD with multi-layered disc springs[4,8,12]. Figure 1 illustrates the basic mechanism of the two-unit VFD. Both the FD and VFD units contain a friction plate, a friction material, disc springs, and a high-tension bolt. However, unlike the FD unit, the VFD unit includes a variable-height component (VHC) consisting of tapered parts and roller bearings; this is the key feature of the VFD unit. When the VFD unit is in the neutral configuration, the height of the VHC is large (Figure 1(a)). As the displacement of VFD unit increases, the height of VHC decreases (Figure 1(b)), thus reducing the compressive force on the friction interface, resulting in a decrease in the frictional sliding force.

Figure 2 shows conceptual diagrams of the restoring force characteristics of the VFD and FD under the same friction sliding forces at neutral displacement. As shown in Figure 2(a), the FD retains a constant sliding force as the device displacement increases, whereas the VFD, shown in Figure 2(b), is designed to produce a reduced sliding force when the device is displaced beyond point P_1. Therefore, in comparison with the installation of an FD in the mainframe of a structure (Figure 2(c)), the installation of the VFD produces a relatively low increase in the stress experienced by the mainframe, even at a large response displacement (Figure 2(d)). The VFD is expected to be especially useful in the case of the seismic retrofitting of existing structures where the strength of the mainframe and foundation is insufficient or unclear for the stress increase due to addition of supplemental friction devices.

3 Variable Friction Damper Experiments

The present experiments expanded on previous studies on the elemental testing and the full-scale loading testing of VFD specimens[43,44] by providing detailed insight into the function and energy response behavior of the VFD devices. The elemental test was carried out using an elemental specimen to grasp the basic characteristics of the VFD units, including their operation behavior. The full-scale tests were conducted by dynamic loading using a brace-type VFD specimen installed in a testing frame, to verify the performance of the VFD. For a past study on a related device in the literature, Downey et al.[40] experimentally investigated a prototype elemental specimen of a cam-based passive variable frictional device that yields a decreased sliding force as the device displacement increases, but they did not evaluate the energy response behavior of the device. On the other hand, the present study investigated the energy response behavior of the VFD based on full-scale experiments using a multi-unit type VFD incorporated into a steel frame.

3.1 Elemental test

3.1.1 Methods of elemental test

The elemental specimen shown in Figure 3 was used in the elemental test. The elemental specimen consisted of two VFD units, each of which included friction plates, friction materials, disc springs, a high-tension bolt, and a VHC. The specifications of the elemental specimen are given in Table 1. A tensile force of 120 kN was applied to each high-tension bolt of the specimen, and the axial force at each bolt was measured by a load cell during the elemental test. In each VFD unit, 12 roller bearings and 12 pairs of tapered parts were incorporated into the VHC. The shape of the tapered parts was designed such that the height of the VHC decreases toward a displacement of 40 mm (point P_2 in Figure 2(b)) when the device displacement exceeds 10 mm (point P_1 in Figure 2(b)). The movement of the roller bearings was synchronized because each roller bearing was sandwiched by the tapered parts under a compressive force, and retainers (as guiding members) installed at each roller bearing enforce synchronization. Therefore, each roller had negligible backlash, slippage, and separation. A unidirectional cyclic loading (triangle waves, maximum velocity of 3 cm/s) was applied to the elemental specimen.

3.1.2 Results of elemental test

The elemental test results (amplitude ±40 mm, five cycles) are shown in Figure 4. Here, the average bolt axial force is the average tensile force measured by the two load cells installed at the high-tension bolts (Section 3.1.1). Figure 4(a) shows the time history of the damper displacement, demonstrating that a triangle wave with an amplitude of ±40 mm was applied to the elemental specimen. The time history waveform of the average bolt axial force, shown in Figure 4(b), indicates that the tensile force of the bolts passively varied depending on the damper displacement (Figure 4(a)) via the operation of the VHC. Figure 4(c) shows the average bolt axial force plotted against the damper displacement in the steady state. This figure demonstrates that the tensile force of the bolts decreased from approximately 120 kN to almost 0 kN after the damper displacement exceeded the predetermined value (= 10 mm) because of the work of the VHC. The time history of the damper force, shown in Figure 4(d), demonstrates that the change in the tensile force of the high-tension bolts (Figure 4(b)) affected the friction sliding force of the elemental specimen (Figure 4(d)). Figure 4(e) shows the relationship between the damper force and the damper displacement in the steady state. From this hysteresis loop, the elemental specimen produced a decreased friction sliding force, as designed, toward a displacement of 40 mm (point P_2 in Figure 2(b)) when the damper displacement exceeded 10 mm (point P_1 in Figure 2(b)).

3.2 Full-scale loading tests

3.2.1 Methods of full-scale tests

Figures 5 and 6(a) show an elevation drawing and a photograph, respectively, of the loading system used for full-scale testing. The loading system mainly consisted of a dynamic 1000-kN actuator for unidirectional loading in the horizontal direction, an H-steel loading beam, an H-steel base beam, two H-steel columns, and a brace-type VFD specimen installed in a diagonal H-steel brace member. Each column was pin-connected to the loading and base beams at both ends. The span between the two columns was 5.0 m, and the span between the loading and base beams was 3.17 m in height. The installation angle of the diagonal brace was 38.4°.

A photograph of the brace-type VFD specimen is shown in Figure 6(b). The number of VFD specimens was one. Figure 7 shows drawings of the VFD specimen. The section geometry of the H-steel member of the VFD specimen was H-400 mm × 362 mm. Figure 8 shows conceptual diagrams of the damper force plotted against the displacement of the VFD specimen and its constituent units in the full-scale loading tests. The VFD specimen consisted of eight VFD units mounted in the flange of the H-steel member and two FD units mounted in the web of the H-steel member. The characteristics of the VFD specimen were obtained as a parallel summation of all the contributions of the constituent VFD and FD units. Each of the VFD and FD units was designed and fabricated so as to produce an initial friction sliding force of approximately 80 kN per unit. Each VFD and FD unit had two friction interfaces, and a target axial force of 120 kN was applied to each high-tension bolt. For each VFD unit, the two displacement points illustrated in Figure 8 were set as follows: the friction sliding force starts to decrease when exceeding a displacement of 10 mm (point P_1 in Figure 8), and the skeleton of the hysteresis loop subsequently decreases toward a displacement of 40 mm (point P_2 in Figure 8). The specifications of the VFD specimen used in the full-scale tests are given in Table 1.

Table 2 gives the program of full-scale loading tests. Runs 1–7 and 10 were sinusoidal loadings with various periods (100, 4.3, and 1.7 s) and target damper displacements (10, 20, 30, and 40 mm). Runs 8 and 9 adopted simulated seismic response story drift waveforms obtained from a response analysis using a multi-degree-of-freedom system supposing a tall building, where the natural periods were 4.3 and 1.7 s for the first and second modes, respectively. Repetitive loading using a 100-cycle sinusoidal wave was used in run 10.

3.2.2 Results of full-scale tests

Figure 9 shows the time history of the damper displacement D_d and the damper force F_d of the VFD specimen obtained from the sinusoidal loadings (runs 2–5) of the full-scale tests. Here, the displacement D_d is the slip displacement at the VFD specimen in the diagonal brace axis direction as measured by displacement meters. Additionally, the force F_d is the axial damper force in the direction of the diagonal brace, which is calculated as follows

$$F_d = F_a/\cos\theta, \qquad (1)$$

where F_a is the load measured at the actuator in the horizontal direction and θ (= 38.4°) is the angle of the diagonal brace axis.

From Figure 9, because the actuator is displaced sinusoidally in the horizontal direction, the resulting damper displacement D_d in the diagonal direction was also sinusoidal. In contrast, the damper force F_d showed non-sinusoidal waveforms because of the nonlinear and variable frictional behavior, and the shape of the waveforms changed as the displacement amplitude was increased from runs 2 to 5.

Figure 10 shows the hysteresis loops of the VFD specimen in the diagonal direction (i.e., relationships of F_d and D_d) obtained from the sinusoidal loadings (runs 2–5). Additionally, the loops in the relationship between the actuator force F_a and the actuator displacement D_a in the horizontal direction are included in Figure 10. This figure demonstrates that the VFD specimen produced a stable displacement-dependent variable friction sliding force and corresponded approximately to the target conceptual hysteresis loop (Figure 8).

Figure 11 plots the energy consumed by the VFD specimen in each cycle of the sinusoidal loadings (runs 2–5). Here, the dissipated energy was calculated from the integration of F_d and the increment of D_d for each cycle. The ratios of the energy of the final cycle to that of the first cycle were 1.009, 1.022, 1.012, and 0.989 for runs 2– 5, respectively. This indicates that the energy response of the VFD specimen was very stable over all cycles, resulting in little change even when the cycle number increased.

Figure 12 shows the dissipated energy of the VFD specimen averaged over all cycles in each run for runs 2–7. Because runs 2 and 6 underwent the different loading periods (4.3 and 1.7 s) but with the same displacement amplitude of 10 mm, the averaged dissipated energies were almost identical. A similar tendency was observed for runs 3 and 7, which were also subjected to the same displacement amplitude (20 mm) with different periods (4.3 and 1.7 s). Figure 13 shows the dissipated energy ratio R_d, defined as the ratio of the energy dissipated by the VFD specimen to that by a theoretical FD with a rectangular hysteresis loop (for runs 2–7). Here, R_d was calculated for each run as

$$R_d = E_d/[2F_{0,ave}(D_{max} - D_{min})], \quad (2)$$

where E_d is the energy dissipated by the VFD specimen averaged over all cycles; $F_{0,ave}$ is the damper force F_d at a neutral displacement (0 mm) averaged over all cycles; and D_{min} and D_{max} are the peak negative and positive damper displacements, respectively.

As shown in Figure 13, as the runs proceeded from runs 2 to 5 and the damper displacement increased, the calculated dissipated energy ratio R_d decreased; R_d for runs 2–5 was 0.941, 0.866, 0.769, and 0.692, respectively. This was because the friction sliding force of the VFD specimen decreased as the damper displacement increased. Moreover, for runs 2 and 6 under the same displacement amplitude of 10 mm, approximately the same R_d (0.941 and 0.968) was calculated despite their different loading periods (4.3 and 1.7 s), and a similar tendency was observed for runs 3 (R_d = 0.866) and 7 (R_d = 0.873) with a displacement amplitude of 20 mm.

Figures 14 and 15 show the coefficient of friction C_f per friction interface of the VFD specimen obtained from the sinusoidal loadings (runs 1–7). Here, C_f was calculated as

$$C_f = F_0/(T_t N_u N_i), \quad (3)$$

where F_0 is the damper force F_d at a neutral displacement (0 mm) averaged for the positive and negative forces in each cycle, T_t (= 120 kN) is the target installation tension applied to each high-tension bolt, N_u (= 10) is the total number of the VFD and FD units, and N_i (= 2) is the number of the friction interfaces.

Figure 14 shows the coefficient of friction C_f plotted against the loading cycle number. This figure indicates that the coefficient of friction C_f of the VFD specimen was adequately stable over the cycles, resulting in less variation with the cycle number. Figure 15 shows the coefficient of friction C_f averaged over all cycles in each run. As shown in this figure, the average C_f fell within the range of approximately 0.30 to 0.34, and the changes were sufficiently small among the runs.

Figures 16–18 show the behaviors of the VFD specimen subjected to the simulated earthquake response story drift waveform loadings (runs 8 and 9). Figures 16 and 17 show the displacement and velocity waveforms, respectively, of the VFD specimen in the brace axis direction. The peak velocities in runs 8 (Figure 17(a)) and 9 (Figure 17(b)) were 16.3 and 20.6 cm/s, respectively. As shown in the damper hysteresis loops (Figure 18), the VFD specimen exhibited stable operation even under the random-like and high-velocity dynamic excitations.

Figure 19 shows the results of the 100-cycle sinusoidal loading (run 10). From Figure 19(a) and (b), the damper hysteresis loops and the time history of the damper force of the VFD specimen demonstrated negligible damper force degradation and a high endurance against the repetitive loadings. From the energy dissipated by the VFD specimen averaged over each set of 10 cycles (Figure 19(c)), a roughly constant energy absorption was observed during the 100 loading cycles. The ratio of the dissipated energy in the last 10 cycles (cycles 91–100) to that in the first 10 cycles (i.e., cycles 1–10) was 0.908, indicating a stable performance and little degradation under repetitive loading.

4 Earthquake Response Analysis

This section presents a nonlinear earthquake response simulation using a building model with VFDs to assess the response control effects. For a related past study, Barzegar et al.[41] numerically evaluated the response of multi-story linear building mainframes with a cam-based device producing a decreased sliding force subjected to wind loads. On the other hand, the present study assessed the energy response behavior of the nonlinear building mainframe incorporating VFDs under various seismic motions including LPLD waves.

4.1 Methods of analysis

A two-dimensional (2D) 30-story steel frame was prepared based on a previously developed three-dimensional frame[49] for use as the mainframe of the numerical structure model in this study.

Three damper case models with identical mainframes, referred as Models VFD, FD, and MF, were investigated. Figure 20(a) depicts the elevation of the 2D frame for Models VFD and FD. For each of the three models, the weight of each story was 2765 kN, and the roof had a weight of 4147 kN. Tables 3 and 4 give the cross-sectional geometry of the columns and girders, respectively, of the mainframe. The bottoms of the columns of the first story were fixed to the ground. The rigid-floor assumption was adopted in the horizontal (X) direction for each floor. As for the bending behavior of the girders, nonlinear single-axis springs with a bilinear restoring force characteristic were set at both ends of each girder. Regarding the columns, to consider the effect of the axial force on the bending behavior, nonlinear axial multi springs with a bilinear restoring force characteristic were set at both ends of each column. The steel had a Young's modulus of 2.05×10^5 MPa and yield strengths of 357.5 MPa (thickness $\leq$ 40 mm) and 324.5 MPa (thickness > 40 mm).

Two diagonal brace-type VFDs were placed in each story of the Model VFD (Figure 20(a)). Figure 20(b) shows a schematic of the restoring force characteristics of each brace-type VFD along the damper axis, including the effect of the stiffness of a brace member in series. Here, K_{d1} is the initial stiffness, F_{d1} is the initial sliding friction force, F_{d2} is the sliding friction force at the point P_2, D_{d1} is the sliding displacement at point P_1, and D_{d2} is the displacement at point P_2. In the analysis, D_{d1} and D_{d2} were set to 8 and approximately 40 mm, respectively. F_{d2} was set to $F_{d2} = 0.1F_{d1}$. The unloading stiffness was the same as the initial stiffness K_{d1}, which was calculated based on the length, cross-sectional area, and Young's modulus of the brace member, under the assumption of an infinite stiffness of the damper portion. Model FD incorporated two diagonal brace-type FDs with an elastic–plastic hysteresis behavior in each story, instead of the VFD. Figure 20(c) shows the restoring force characteristics of the FD in the damper axis. The K_{d1} and F_{d1} values applied to the dampers in each story in Model FD were the same as those used in Model VFD. Table 5 gives the properties of the dampers in each story, along with the brace members placed in series, for Models VFD and FD. Model MF contained no dampers, only the mainframe.

Three groups of input motions were used in the analysis: simulated waves, observed records, and LPLD ground motions. Table 6 lists the input motions. Figure 21 shows the velocity response spectra (damping factor 5%) of the input motions. For the simulated waves, five waveforms[50], referred to as waves M1–M5, were used. Each of the simulated waves was prepared such that the pseudo velocity response spectrum (damping factor 5%) was constant when the period exceeded 0.64 s, the phase characteristics were given by random numbers, and the duration of the steady portion in the time domain was 30 s. The original waves M1–M5 were amplified by an input multiplier of 1.5 and used as the input motions. For the observation records, five waveforms, referred to as waves Elcn, Taft, Hach, Tohk, and Kobe, were used. These waves were the N–S directional components of the El Centro 1940, Taft 1952, Hachinohe 1968, Tohoku 1978, and Kobe 1995 earthquake records provided by the Building Performance Standardization Association[51] and the Japan Meteorological Agency[52]. Each of the observed records was normalized such that the peak ground velocity (PGV) was equal to 0.75 m/s for use in the analysis. For the LPLD ground motions, five waveforms, referred to as waves LPLD1–LPLD5, were prepared. Each of the LPLD waves was prepared such that response spectrum was increased in the range of natural periods of 2.5–6.0 s [53], the phase characteristics were given by random numbers, and the duration of the steady portion in the time domain was 180 s. Each of the original LPLD waves was amplified by an input multiplier of 1.25 and used as the input motion.

For structural damping, Rayleigh damping was applied with a damping ratio of 0.015 for each of the first and second modes. The Newmark-beta method (beta = 1/4) was employed in the time history numerical integration with a time interval of 0.002 s.

4.2 Results of analysis

The natural period for the first vibration mode obtained from an eigenvalue analysis was 4.18 s for Model MF and 3.18 s for both Models FD and VFD. Because the same initial stiffness was set for the brace-type FDs and VFDs, the same natural periods were obtained in Models FD and VFD. As a result of an enhancement in the elastic stiffness, the natural period for Models FD and VFD was 76.0% of that without dampers (Model MF).

Figure 22 shows the peak story drift response for the three input motion groups (the simulated waves, observed records, and LPLD ground motions) and the three models (Models MF, FD, and VFD). Here, the maximum value of the peak story drift in each input motion group is plotted for each story. The peak story drift ratio (the maximum value across all stories in each input motion group) of Models MF, FD, and VFD, respectively, were as follows: 4.03%, 1.19%, and 1.21% under the simulated waves; 1.82%, 1.03%, and 1.07% under the observed records; and 3.41%, 1.20%, and 1.22% under the LPLD ground motions. From these results, incorporating the brace-type FDs and VFDs significantly reduced the peak story drift in Models FD and VFD in comparison with that in Model MF. Although the peak story drift in the lower stories of Model VFD was larger than that in Model FD, the maximum value across all stories in Model VFD was not significantly higher than that in Model FD.

Figure 23 shows the peak story shear force response for the three input motion groups and the three models. Here, the maximum value of the peak story shear force in each input motion group is plotted. The peak base shear response (the maximum value in each input motion group) for Models MF, FD, and VFD, respectively, were as follows: 6.83, 10.36, and 9.50 MN under the simulated waves; 7.07, 10.06, and 9.53 MN under the observed records; and 7.04, 9.62, and 9.37 MN under the LPLD ground motions. From the results, the peak base shear of Model VFD was clearly lower than that of Model FD. This is attributable to the reduction in the sliding friction force by the work of the brace-type VFDs incorporated into Model VFD. Additionally, Figure 24 shows the peak story shear coefficient response for the three input motion groups and the three models (maximum value in each input motion group). This figure shows a tendency similar to that shown in Figure 23.

Figure 25(a) and (b) shows the ratios of the hysteretic energy absorbed by the mainframe and that absorbed by the dampers (brace-type FDs and VFDs), respectively, to the total input energy for each of the three models. Here, the mainframe hysteretic energy was the sum of the energy over all girders and columns in all stories, and the damper hysteretic energy was the sum of the energy over all dampers in all stories. The total input energy was obtained as the sum of the hysteretic energies absorbed by the mainframe and dampers and the energy consumption by the Rayleigh damping (Section 4.1). Each energy ratio was averaged in each input motion group. In the figure, SW, OR, and LPLD for the input motion groups denote the simulated waves, observed records, and LPLD ground motions, respectively. From Figure 25(a), the energy ratio for the mainframe of Models FD and VFD was substantially lower than in the case without dampers (Model MF) because of the supplemental energy dissipation effects by the dampers (Figure 25(b)). This implies that the damage to the mainframe would be decreased by incorporating brace-type FDs and VFDs. Moreover, for both the mainframe (Figure 25(a)) and the dampers (Figure 25(b)), the energy ratio for Model VFD was approximately the same as that for Model FD. The reason for this approximately equal energy response by Models FD and VFD is assumed to be that the damper displacement of the VFDs was larger than that of the FDs when a lower frictional sliding force was produced in the VFDs.

Regarding the column axial force response behavior, the peak axial compressive force of the first-story columns at the damper installation span in the vertical direction for Model FD (the maximum value over all columns and all 15 input motions) was 28.03 MN, whereas that for Model VFD was 26.80 MN; thus, the ratio of the column axial force for Model VFD to that for Model FD was 0.956. This indicates that incorporating brace-type VFDs can mitigate the increase of the column axial force that can result from installing conventional FDs.

Table 7 shows the mean, standard deviation (SD), and coefficient of variation (CV) of the peak responses of Models MF, FD, and VFD for each of the input motion groups (SW, OR, and LPLD) obtained from the numerical simulation. Here, the peak responses are the peak acceleration averaged for all stories, peak story drift averaged for all stories, and peak base shear. Also, Table 8 gives the mean, SD, and CV for the corresponding energy ratios. Here, the ‘energy ratio of mainframe’ is the ratio of the hysteretic energy dissipated by the mainframe to the total input energy obtained as the summation of all members in all stories. Similarly, ‘energy ratio of dampers’ is the ratio of the hysteretic energy dissipated by the dampers to the total input energy obtained as the summation of all members in all stories. From these results, the mean of the peak story drift for Model VFD was significantly reduced compared with that for Model MF. Moreover, Model VFD showed lower mean of the peak base shear than Model FD while showing roughly the same mean of the peak story drift as Model FD. As for the variation in the peak responses and energy ratios, the obtained SD and CV for Model VFD showed no clear tendency of the differences compared with those for Model FD. One possible reason for the unclear tendency of differences in variation (SD and CV) for Model VFD compared with Model FD is that the device displacement of the VFD averaged for all stories basically did not exceed the point P_2 in Figure 20(b) in the present analysis. However, it should be noted that if the device response displacement of the VFD greatly exceeds the point P_2 in Figure 20(b) due to an excessive seismic input, the energy absorption performance of the VFD is reduced. In that case, as well as the peak story drift, the variation such as SD for the peak responses of Model VFD may increase.

5 Conclusions

In this study, a passive VFD with a displacement-dependent friction sliding force characteristic was studied. The energy response behavior of the VFD specimen was investigated based on full-scale dynamic loading tests results. Additionally, a seismic response simulation was conducted with a 2D 30-story nonlinear mainframe model with the VFDs incorporated into each story under various input motions, including simulated waves, observed records, and LPLD ground motions. The following conclusions can be drawn from this study.

1) From the full-scale loading tests, the VFD specimen produced a lower friction sliding force when the damper displacement exceeded a predetermined value and the VHC became activated, resulting in a reduction in the dissipated energy ratio as the damper displacement increased.
2) The VFD specimen exhibited stable energy response behavior as well as a stable friction sliding force and friction coefficient under the considered loadings: sinusoidal waves, random-like seismic response waves, and a 100-cycle repetitive wave.
3) The energy response behavior of the VFD specimen was almost independent of the loading frequency, showing less velocity-dependent characteristics, under the given experimental conditions.
4) From the numerical earthquake response simulation using the 2D nonlinear frame model, the peak story drift response of the case with the brace-type VFDs was not significantly higher than in the case with the FDs. The dissipated energy ratios of the mainframe and dampers for the case with the VFDs were roughly identical to those for the case with the FDs.
5) The numerical simulation demonstrated that the brace-type VFD can yield a lower peak story shear force response than in the case with conventional FDs. This was true under various input motions, including motions from observation records and LPLD ground motions. Moreover, with VFDs installed, the maximum column compressive axial force of the first story at the damper installation span is less than that when FDs are installed.

Acknowledgments

The present study was supported in part by the Japan Society for the Promotion of Science, KAKENHI Grant Number JP19H02279. The observation data used in the numerical simulation were provided by the Building Performance Standardization Association and the

Japan Meteorological Agency.

References

1. Pall AS, Marsh C. Response of friction damped braced frames. *Journal of the Structural Division (ASCE)* 1982; 108(6): 1313–1323.
2. Mualla IH, Belev B. Performance of steel frames with a new friction damper device under earthquake excitation. *Engineering Structures* 2002; 24(3): 365–371. https://doi.org/10.1016/S0141-0296(01)00102-X
3. Morgen BG, Kurama YC. Seismic design of friction-damped precast concrete frame structures. *Journal of Structural Engineering (ASCE)* 2007; 133(11): 1501–1511. https://doi.org/10.1061/(ASCE)0733-9445(2007)133:11(1501)
4. Suzui Y, Sano T, Nomura J, Utsumi Y. Development of advanced brake damper. *Report of Obayashi Corporation Technical Research Institute* 2009; 73: 1−6. (in Japanese).
5. Dal Lago B, Biondini F, Toniolo G. Friction-based dissipative devices for precast concrete panels. *Engineering Structures* 2017; 147: 356–371. https://doi.org/10.1016/j.engstruct.2017.05.050
6. Shirai K, Kikuchi M, Ito T, Ishii K. Earthquake response analysis of the historic reinforced concrete temple Otaniha Hakodate Betsuin after seismic retrofitting with friction dampers. *International Journal of Architectural Heritage* 2018; 13(1): 47–57. https://doi.org/10.1080/15583058.2018.1497222
7. Tsampras G, Sause R, Fleischman RB, Restrepo JI. Experimental study of deformable connection consisting of friction device and rubber bearings to connect floor system to lateral force resisting system. *Earthquake Engineering and Structural Dynamics* 2018; 47(4): 1032–1053. https://doi.org/10.1002/eqe.3004
8. Sano T, Shirai K, Suzui Y, Utsumi Y. Loading tests of a brace-type multi-unit friction damper using coned disc springs and numerical assessment of its seismic response control effects, *Bulletin of Earthquake Engineering* 2019; 17(9): 5365–5391. https://doi.org/10.1007/s10518-019-00671-8
9. Shirai K, Nagaoka A, Fujita N, Fujimori T. Optimal damper slip force for vibration control structures incorporating friction device with sway-rocking motion obtained using shaking table tests. *Advances in Civil Engineering* 2019: Article ID 6356497. https://doi.org/10.1155/2019/6356497
10. Taiyari F, Mazzolani FM, Bagheri S. Damage-based optimal design of friction dampers in multistory chevron braced steel frames. *Soil Dynamics and Earthquake Engineering* 2019; 119: 11–20. https://doi.org/10.1016/j.soildyn.2019.01.004
11. Jarrahi H, Asadi A, Khatibinia M, Etedali S. Optimal design of rotational friction dampers for improving seismic performance of inelastic structures. *Journal of Building Engineering* 2020; 27: 100960. https://doi.org/10.1016/j.jobe.2019.100960
12. Sano T, Shirai K, Suzui Y, Utsumi Y. Dynamic loading tests and seismic response analysis of a stud-type damper composed of multiple friction units with disc springs. *Earthquake Engineering and Structural Dynamics* 2020; 49(13): 1259–1280. https://doi.org/10.1002/eqe.3289
13. Xue J, Wu C, Zhang X, Qi Z. Experimental and numerical analysis on seismic performance of straight-tenon joints reinforced with friction damper. *Structural Control and Health Monitoring* 2020; 27(10): e2613. https://doi.org/10.1002/stc.2613
14. Saingam P, Matsuzaki R, Nishikawa K, Sitler B, Terazawa Y, Takeuchi T. Experimental dynamic characterization of friction brace dampers and application to the seismic retrofit of RC buildings. *Engineering Structures* 2021; 242: 112545. https://doi.org/10.1016/j.engstruct.2021.112545
15. Shirai K, Horii J, Fujimori T. Optimal sliding force characteristics of friction dampers for seismic response control of building structures considering sway-rocking motion. *Soil Dynamics and Earthquake Engineering* 2021; 149: 106892. https://doi.org/10.1016/j.soildyn.2021.106892
16. Fujita T, Kabeya K, Hayamizu Y, Aizawa S, Higashino M, Kubo T, Haniuda N, Mori T. Semi-active seismic isolation system using controllable friction damper: 1st report, development of controllable friction damper and fundamental study of semi-active control system. *Transactions of the Japan Society of Mechanical Engineers* 1991; C57(536): 1122–1128. (in Japanese). https://doi.org/10.1299/kikaic.57.1122
17. Feng MQ, Shinozuka M, Fujii S. Friction-controllable sliding isolation system. *Journal of Engineering Mechanics* 1993; 119(9): 1845-1864. https://doi.org/10.1061/(ASCE)0733-9399(1993)119:9(1845)
18. Nagarajaiah S, Feng MQ, Shinozuka M. Control of structures with friction controllable sliding isolation bearings. *Soil Dynamics and Earthquake Engineering* 1993; 12(2): 103–112. https://doi.org/10.1016/0267-7261(93)90049-W
19. Kannan S, Uras HM, Aktan HM. Active control of building seismic response by energy dissipation. *Earthquake Engineering and Structural Dynamics* 1995; 24(5): 747–759.

https://doi.org/10.1002/eqe.4290240510

20. Inaudi JA. Modulated homogeneous friction: a semi-active damping strategy. *Earthquake Engineering and Structural Dynamics* 1997; 26(3): 361–376. https://doi.org/10.1002/(SICI)1096-9845(199703)26:3<361::AID-EQE648>3.0.CO;2-M
21. Nishitani A, Nitta Y, Ishibashi Y, Itoh A. Semi-active structural control with variable friction dampers. *Proceedings of the 1999 American Control Conference* 1999: 1017–1021. https://doi.org/10.1109/ACC.1999.783194
22. Lu LY. Predictive control of seismic structures with semi-active friction dampers. *Earthquake Engineering and Structural Dynamics* 2004; 33(5): 647–668. https://doi.org/10.1002/eqe.371
23. Narasimhan S, Nagarajaiah S. Smart base isolated buildings with variable friction systems: $H\infty$ controller and SAIVF device. *Earthquake Engineering and Structural Dynamics* 2006; 35(8): 921–942. https://doi.org/10.1002/eqe.559
24. Ng CL, Xu YL. Semi-active control of a building complex with variable friction dampers. *Engineering Structures* 2007; 29(6): 1209–1225. https://doi.org/10.1016/j.engstruct.2006.08.007
25. Downey A, Cao L, Laflamme S, Taylor D, Ricles J. High capacity variable friction damper based on band brake technology. *Engineering Structures* 2016; 113: 287–298. https://doi.org/10.1016/j.engstruct.2016.01.035
26. Gong Y, Cao L, Laflamme S, Quiel S, Ricles J, Taylor D. Characterization of a novel variable friction connection for semiactive cladding system. *Structural Control and Health Monitoring* 2018; 25(6): e2157. https://doi.org/10.1002/stc.2157
27. Amjadian M, Agrawal AK. Feasibility study of using a semiactive electromagnetic friction damper for seismic response control of horizontally curved bridges. *Structural Control and Health Monitoring* 2019; 26(4): e2333. https://doi.org/10.1002/stc.2333
28. Gong Y, Cao L, Laflamme S, Ricles J, Quiel S, Taylor D. Variable friction cladding connection for seismic mitigation. *Engineering Structures* 2019; 189: 243–259. https://doi.org/10.1016/j.engstruct.2019.03.066
29. Roik K, Dorka U, Dechent P. Vibration control of structures under earthquake loading by three-stage friction-grip elements. *Earthquake Engineering and Structural Dynamics* 1988; 16(4): 501–521. https://doi.org/10.1002/eqe.4290160404
30. FitzGerald TF, Anagnos T, Goodson M, Zsutty T. Slotted bolted connections in aseismic design for concentrically braced connections. *Earthquake Spectra* 1989; 5(2): 383–391. https://doi.org/10.1193/1.1585528
31. Nims DK, Richter PJ, Bachman RE. The use of the energy dissipating restraint for seismic hazard mitigation. *Earthquake Spectra* 1993; 9(3): 467–489. https://doi.org/10.1193/1.1585725
32. Kar R, Rainer JH, Lefrancois AC. Dynamic properties of a circuit breaker with friction-based seismic dampers. *Earthquake Spectra* 1996; 12(2): 297–314. https://doi.org/10.1193/1.1585881
33. Filiatrault A, Tremblay R, Kar R. Performance evaluation of friction spring seismic damper. *Journal of Structural Engineering (ASCE)* 2000; 126(4): 491–499. https://doi.org/10.1061/(ASCE)0733-9445(2000)126:4(491)
34. Yang TY, Xu HC, Tobber L. Mechanism and experimental validation of innovative self-centering conical friction damper. *Structural Control and Health Monitoring* 2020; 27(10): e2609. https://doi.org/10.1002/stc.2609
35. Ribakov Y. Using viscous and variable friction dampers for improving structural seismic response. *The Structural Design of Tall and Special Buildings* 2011; 20(5): 579-593. https://doi.org/10.1002/tal.629
36. Pranesh M, Sinha R. VFPI: an isolation device for aseismic design. *Earthquake Engineering and Structural Dynamics* 2000; 29(5): 603–627. https://doi.org/10.1002/(SICI)1096-9845(200005)29:5<603::AID-EQE927>3.0.CO;2-W
37. Tsai CS, Chiang TC, Chen BJ. Finite element formulations and theoretical study for variable curvature friction pendulum system. *Engineering Structures* 2003; 25(14): 1719–1730. https://doi.org/10.1016/S0141-0296(03)00151-2
38. Panchal VR, Jangid RS. Variable friction pendulum system for near-fault ground motions. *Structural Control and Health Monitoring* 2008; 15(4): 568–584. https://doi.org/10.1002/stc.216
39. Wang G, Wang Y, Yuan J, Yang Y, Wang D. Modeling and experimental investigation of a novel arc-surfaced frictional damper. *Journal of Sound and Vibration* 2017; 389: 89–100. https://doi.org/10.1016/j.jsv.2016.11.019
40. Downey A, Theisen C, Murphy H, Anastasi N, Laflamme S. Cam-based passive variable friction device for structural control. *Engineering Structures* 2019; 188: 430–439. https://doi.org/10.1016/j.engstruct.2019.03.032
41. Barzegar V, Laflamme S, Downey A, Li M, Hu C. Numerical evaluation of a novel passive variable

friction damper for vibration mitigation. *Engineering Structures* 2020; 220: 110920. https://doi.org/10.1016/j.engstruct.2020.110920
42. Zhao G, Ma Y, Yang Z, Wang Q, Li Y. Friction mechanism and experimental investigation of the response-amplified friction damper. *Structural Control and Health Monitoring* 2022; 29(7): e2953. https://doi.org/10.1002/stc.2953
43. Shirai K, Sano T, Suzui Y, Kageyama M, Kikuchi M. Development of friction damper with displacement dependent variable damping force characteristics. *AIJ Journal of Technology and Design* 2012; 18(38): 85−90. (in Japanese). https://doi.org/10.3130/aijt.18.85
44. Shirai K, Sano T, Suzui Y. Development of a passive variable friction damper with displacement-dependent damping force characteristics. *13th East Asia-Pacific Conference on Structural Engineering and Construction (EASEC-13)* 2013; A-1-1: 1−6.
45. Ito T, Shirai K, Kikuchi M, Sano T. Response control effectiveness of high-rise building using passive variable friction dampers. *13th World Conference on Seismic Isolation, Energy Dissipation and Active Vibration Control of Structures (13WCSI)* 2013; 102: 1–8.
46. Ito T, Shirai K, Kikuchi M, Sano T. An analytical study on earthquake response control effects of a high-rise steel building using variable friction dampers. *Steel Construction Engineering* 2014; 21(84): 57–65. (in Japanese). https://doi.org/10.11273/jssc.21.84_57
47. Shirai K, Ishii A, Kikuchi M. An analytical study on flexural deformation control effects of steel super high-rise buildings using variable friction dampers subjected to earthquakes. *Steel Construction Engineering* 2016; 23(90): 89–104. (in Japanese). https://doi.org/10.11273/jssc.23.90_89
48. Shirai K, Li Y, Ishii A, Kikuchi M. An analytical study on earthquake response control effects of steel super high-rise buildings using variable friction damper with displacement overshoot control mechanism. *Journal of Structural Engineering (AIJ)* 2017; 63B: 153–160. (in Japanese).
49. Koshika N, Suzuki Y. Vibration and structural damage of high-rise buildings. *Open research meeting on countermeasures against long-period ground motions*, Working Group of Countermeasures of Long-period Buildings Against Earthquakes, Structural Committee, Architectural Institute of Japan: 139–140; 2011. (in Japanese).
50. Shirai K, Inoue N. A seismic response estimation method for RC structures using random vibration theory. *Journal of Advanced Concrete Technology* 2014; 12(2): 62–72. https://doi.org/10.3151/jact.12.62
51. Building Performance Standardization Association. (Accessed July 2019). (in Japanese). https://www.seinokyo.jp/jsh/top/
52. Japan Meteorological Agency. (Accessed 30 July 2019). (in Japanese). https://www.data.jma.go.jp/svd/eqev/data/kyoshin/jishin/hyogo_nanbu/index.html
53. Yoshimura C, Yamamoto Y, Kimura Y, Aono H. Target huge earthquakes and areas. *Open research meeting on countermeasures against long-period ground motions*, Working Group of Countermeasures of Long-period Buildings Against Earthquakes, Structural Committee, Architectural Institute of Japan: 129–131; 2011. (in Japanese).

Table 1 Specifications of the variable friction damper (VFD) specimens

	Elemental test	Full-scale tests
Number of friction interfaces	2	2
Disk springs	∅130 mm (SUP10)	∅130 mm (SUP10)
Layer number of disc springs	12 layered in parallel	11 layered in parallel
Bolts	high-tension bolt M27	high-tension bolt M27
Target installation tension	120 kN	120 kN
Friction plates	PL-2 (SUS304)	PL-2 (SUS304)
Friction materials	t 4.3 mm (composite of steel plate and phenolic resin material)	t 4.3 mm (composite of steel plate and phenolic resin material)
Target friction coefficient	approximately 0.39	approximately 0.32

Table 2 Loading program of the full-scale tests[43]

Run	Type of wave	Period of sine wave [s]	Target damper displacement [mm]	Target damper velocity [cm/s]	Steady cycle number
1	Sine wave	100	±10	±0.063	2
2	Sine wave	4.3	±10	±1.46	10
3	Sine wave	4.3	±20	±2.92	10
4	Sine wave	4.3	±30	±4.38	10
5	Sine wave	4.3	±40	±5.84	10
6	Sine wave	1.7	±10	±3.70	10
7	Sine wave	1.7	±20	±7.39	10
8	Simulated earthquake response wave (Kokuji-wave, phase angle 1995 Kobe NS)				
9	Simulated earthquake response wave (1978 Tohoku University NS)				
10	Sine wave	4.3	±40	±5.84	100

Table 3 Cross-sectional geometry of the columns[49] used in the numerical seismic response simulation

Story	Section [mm]
22–30	□-600 × 600 × 19 × 19
19–21	□-600 × 600 × 22 × 22
16–18	□-600 × 600 × 25 × 25
7–15	□-600 × 600 × 32 × 32
4–6	□-600 × 600 × 40 × 40
1–3	□-600 × 600 × 45 × 45

Table 4 Cross-sectional geometry of the girders[49] used in the numerical seismic response simulation

Floor	Section [mm]
26–R	H-850 × 200 × 16 × 19
20–25	H-850 × 250 × 16 × 19
17–19	H-850 × 250 × 16 × 22
14–16	H-850 × 300 × 16 × 22
2–13	H-850 × 300 × 16 × 25

Table 5 Friction sliding force of the brace-type dampers [variable friction damper (VFD) and conventional friction damper (FD)] in the axial direction and cross-sectional geometry of the brace members used in the numerical seismic response simulation

Story	Force [kN]	Section [mm]
28–30	600	H-350 × 350 × 16 × 19
10–27	1200	H-500 × 350 × 19 × 22
7–9	1500	H-500 × 350 × 19 × 22
4–6	1800	H-500 × 350 × 19 × 22
2–3	2200	H-500 × 350 × 19 × 22
1	2200	H-500 × 350 × 22 × 28

Table 6 Input motions used in the numerical seismic response simulation

Input motion group	Wave name	PGA [m/s^2]
Simulated waves (input multiplier = 1.5)	M1	6.285
	M2	5.700
	M3	5.085
	M4	5.085
	M5	4.710
Observed records (N–S direction component, PGV = 0.75 m/s)	Elcn	7.650
	Taft	7.295
	Hach	5.007
	Tohk	5.347
	Kobe	6.690
LPLD ground motions (input multiplier = 1.25)	LPLD1	3.989
	LPLD2	3.907
	LPLD3	4.181
	LPLD4	4.006
	LPLD5	4.261

PGA: Peak ground acceleration
PGV: Peak ground velocity
LPLD: Long-period, long-duration

Table 7 Mean, standard deviation (SD), and coefficient of variation (CV) for the peak responses obtained from the numerical seismic response simulation

Peak response	Input motion group		Model MF	Model FD	Model VFD
Peak acceleration averaged for all stories	SW	Mean [m/s^2]	3.59	4.15	4.07
		SD [m/s^2]	0.286	0.182	0.110
		CV	0.080	0.044	0.027
	OR	Mean [m/s^2]	4.51	4.40	4.34
		SD [m/s^2]	0.567	0.594	0.626
		CV	0.126	0.135	0.144
	LPLD	Mean [m/s^2]	3.18	3.70	3.70
		SD [m/s^2]	0.101	0.105	0.110
		CV	0.032	0.028	0.030
Peak story drift averaged for all stories	SW	Mean [mm]	51.9	32.5	32.4
		SD [mm]	10.68	4.48	4.32
		CV	0.206	0.138	0.133
	OR	Mean [mm]	32.1	25.0	24.8
		SD [mm]	4.48	4.46	4.34
		CV	0.140	0.178	0.175
	LPLD	Mean [mm]	53.7	31.5	31.9
		SD [mm]	4.90	2.12	2.06
		CV	0.091	0.067	0.065
Peak base shear	SW	Mean [MN]	6.55	9.64	9.28
		SD [MN]	0.178	0.382	0.186
		CV	0.027	0.040	0.020
	OR	Mean [MN]	6.55	9.56	9.20
		SD [MN]	0.303	0.320	0.210
		CV	0.046	0.034	0.023
	LPLD	Mean [MN]	6.78	9.48	9.19
		SD [MN]	0.221	0.114	0.116
		CV	0.033	0.012	0.013

SW: For the five simulated waves
OR: For the five observed records
LPLD: For the five long-period, long-duration ground motions

Table 8 Mean, SD, and CV for the energy ratios obtained from the numerical seismic response simulation

Energy ratio	Input motion group		Model MF	Model FD	Model VFD
Energy ratio of mainframe	SW	Mean	0.795	0.505	0.505
		SD	0.014	0.019	0.019
		CV	0.018	0.037	0.038
	OR	Mean	0.703	0.461	0.460
		SD	0.043	0.076	0.076
		CV	0.062	0.165	0.165
	LPLD	Mean	0.809	0.547	0.546
		SD	0.016	0.012	0.012
		CV	0.020	0.022	0.022
Energy ratio of dampers	SW	Mean	-	0.323	0.325
		SD	-	0.011	0.012
		CV	-	0.033	0.036
	OR	Mean	-	0.333	0.334
		SD	-	0.062	0.063
		CV	-	0.186	0.188
	LPLD	Mean	-	0.279	0.281
		SD	-	0.016	0.017
		CV	-	0.059	0.059

SW: For the five simulated waves
OR: For the five observed records
LPLD: For the five long-period, long-duration ground motions

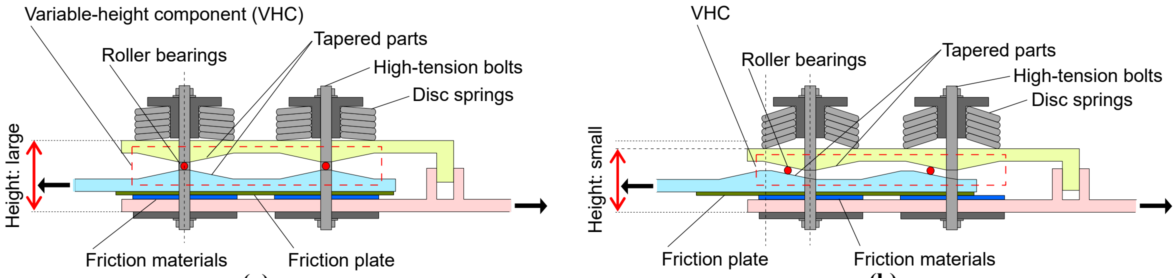

(a) (b)

Figure 1 Schematic of the basic configuration of the two-unit variable friction damper (VFD): **(a)** in the neutral configuration; and **(b)** in a displaced configuration

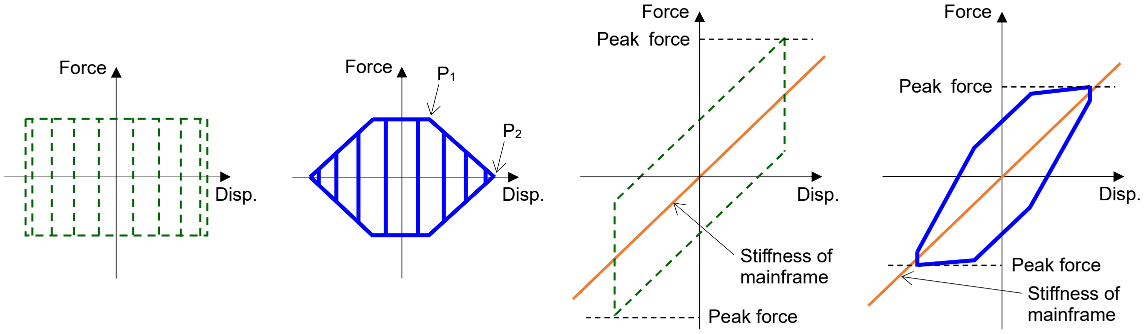

(a) (b) (c) (d)

Figure 2 Conceptual diagrams of the hysteretic loops: **(a)** conventional friction damper (FD) alone; **(b)** variable friction damper (VFD) alone; **(c)** mainframe incorporating the FD; and **(d)** mainframe incorporating the VFD

(a) (b)

Figure 3 Photographs of the elemental test specimen consisting of two variable friction damper (VFD) units: **(a)** front view[43]; and **(b)** side view

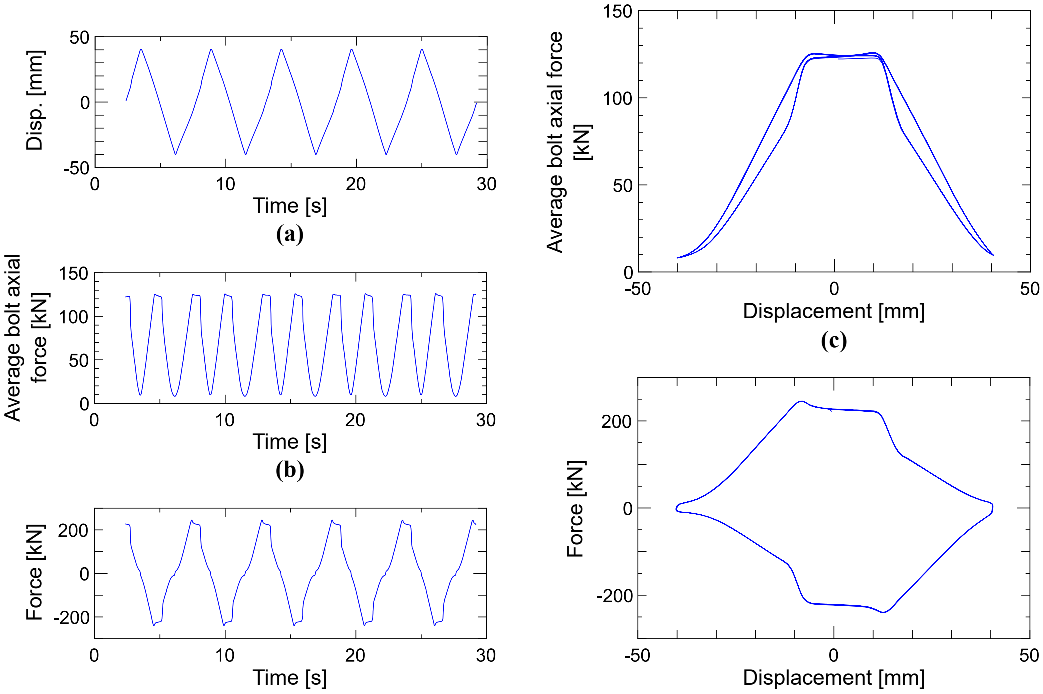

(a) (b) (c) (d) (e)

Figure 4 Results of the elemental test (triangle waves, loading amplitude ±40 mm, maximum loading velocity 3 cm/s, five cycles): **(a)** time history of the damper displacement; **(b)** time history of the average bolt axial force; **(c)** average bolt axial force plotted against damper displacement (steady portion); **(d)** time history of the damper force; and **(e)** hysteresis loop of the damper[43] (steady portion)

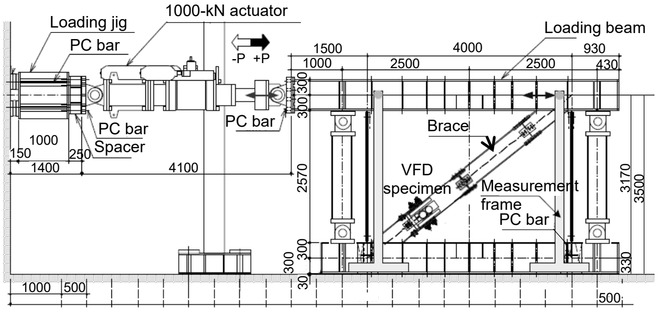

[Unit: mm]

Figure 5 Elevation drawing of the loading system incorporating the brace-type variable friction damper (VFD) specimen for full-scale testing[43]

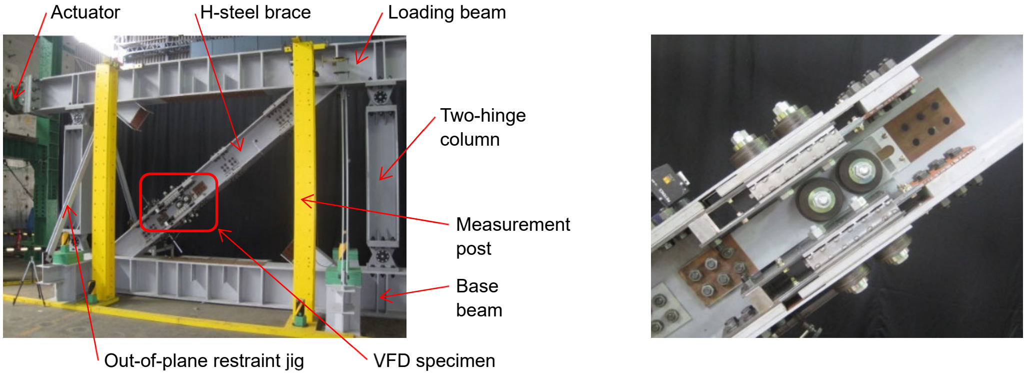

(a) (b)

Figure 6 Photographs of the full-scale testing setup: **(a)** dynamic loading system[44]; and **(b)** variable friction damper (VFD) specimen

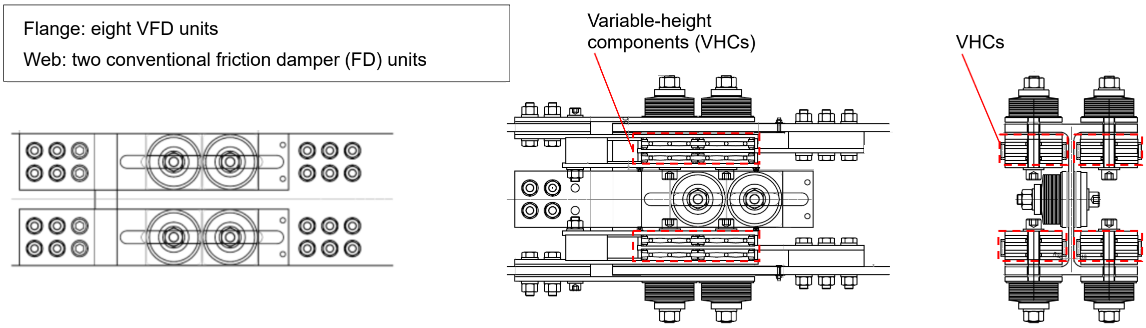

(a) (b) (c)

Figure 7 Drawings of the variable friction damper (VFD) specimen used in the full-scale tests[44]: **(a)** plan view of the flange part; **(b)** side view of the web part; and **(c)** section view

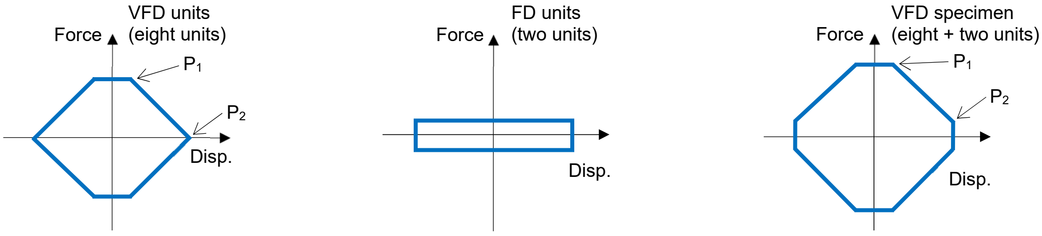

(a) (b) (c)

Figure 8 Schematics of the force–displacement relationship of the variable friction damper (VFD) specimen: **(a)** contribution of the VFD units; **(b)** contribution of the conventional friction damper (FD) units; and **(c)** hysteresis loop of the full VFD specimen (i.e., sum of the contributions of the VFD and FD units)

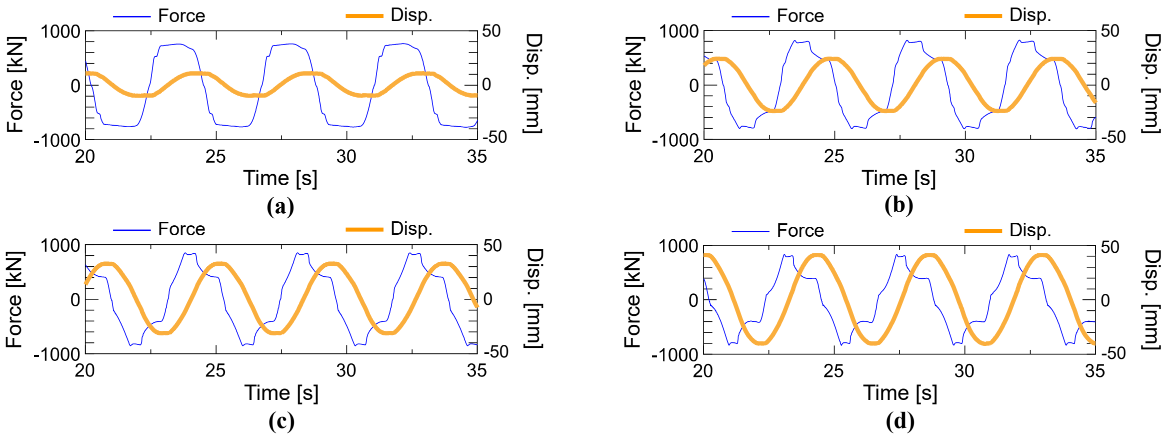

Figure 9 Time history of the damper force F_d and damper displacement D_d of the variable friction damper (VFD) specimen under sinusoidal loadings in full-scale tests: **(a)** run 2; **(b)** run 3; **(c)** run 4; and **(d)** run 5

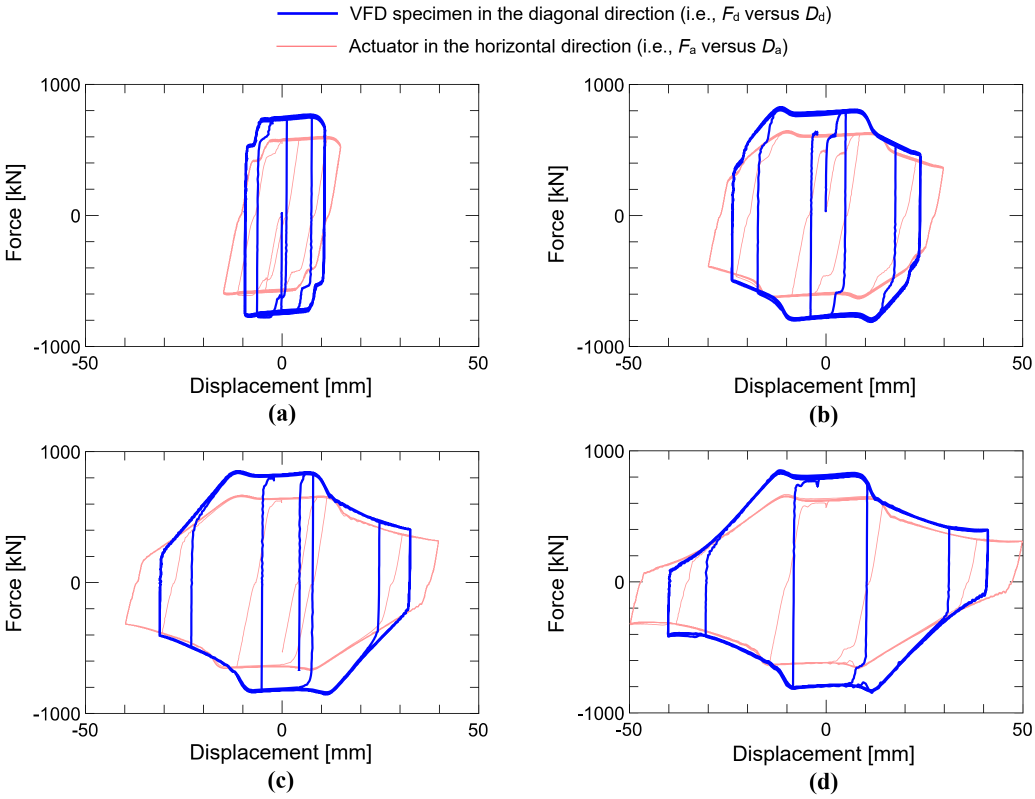

Figure 10 Hysteresis loops of the variable friction damper (VFD) specimen in the diagonal direction and the actuator in the horizontal direction for the sinusoidal loadings obtained from the full-scale tests: **(a)** run 2; **(b)** run 3; **(c)** run 4 [43]; and **(d)** run 5

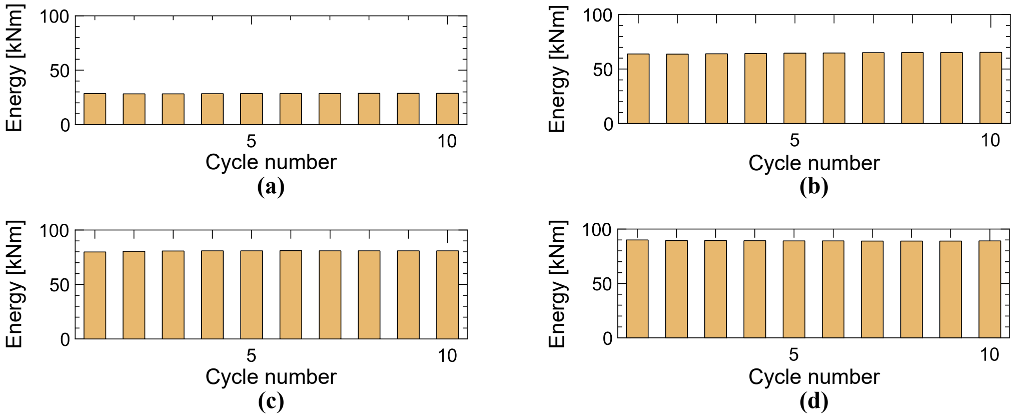

Figure 11 Hysteretic energy dissipated by the variable friction damper (VFD) specimen for each cycle of the sinusoidal loadings of the full-scale tests: **(a)** run 2; **(b)** run 3; **(c)** run 4; and **(d)** run 5

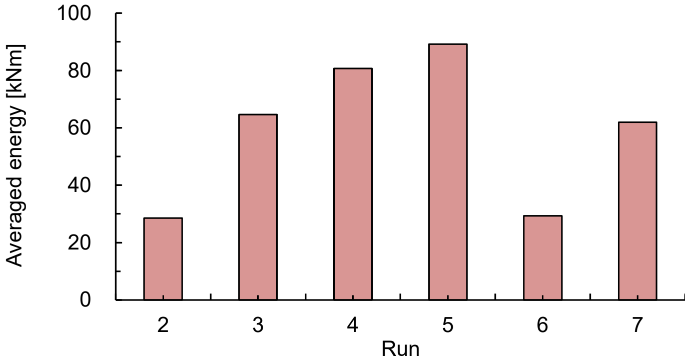

Figure 12 Hysteretic energy dissipated by the variable friction damper (VFD) specimen averaged over all cycles in each of the sinusoidal loadings (runs 2–7) in the full-scale tests

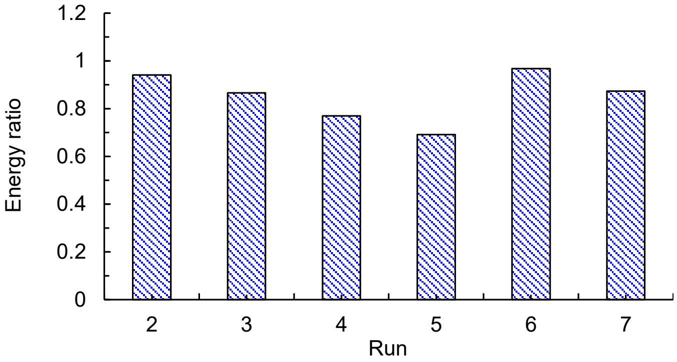

Figure 13 Ratio of the energy dissipated by the variable friction damper (VFD) specimen to that by a theoretical conventional friction damper (FD) averaged over all cycles in each of the sinusoidal loadings (runs 2–7) obtained from the full-scale tests

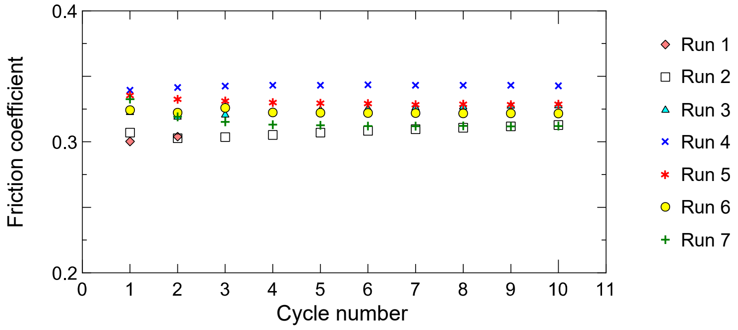

Figure 14 Friction coefficient per sliding surface for each cycle of the sinusoidal loadings (runs 1–7) in the full-scale tests

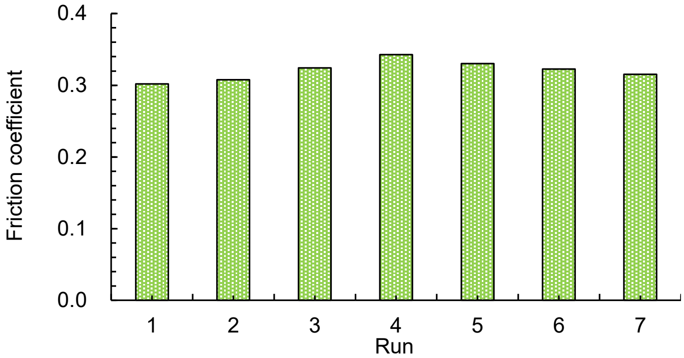

Figure 15 Friction coefficient per sliding surface averaged over all cycles in each of the sinusoidal loadings (runs 1–7) in the full-scale tests

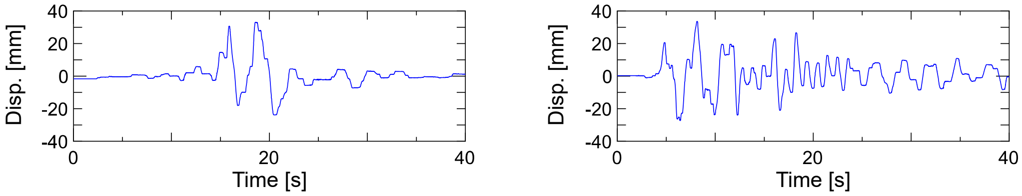

(a)

(b)

Figure 16 Time history of the damper displacement of the variable friction damper (VFD) specimen for the earthquake response wave loadings in the full-scale tests[44]: **(a)** run 8; and **(b)** run 9

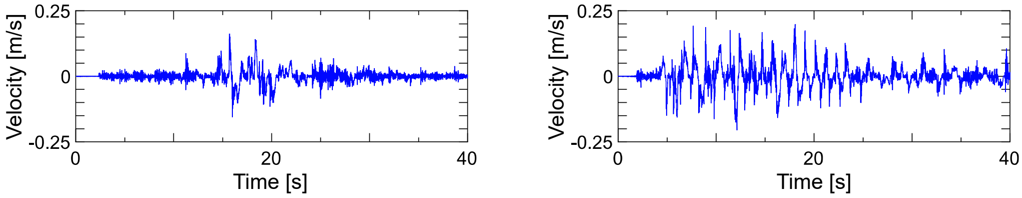

(a) **(b)**

Figure 17 Time history of the damper velocity of the variable friction damper (VFD) specimen for the earthquake response wave loadings in the full-scale tests: **(a)** run 8; and **(b)** run 9

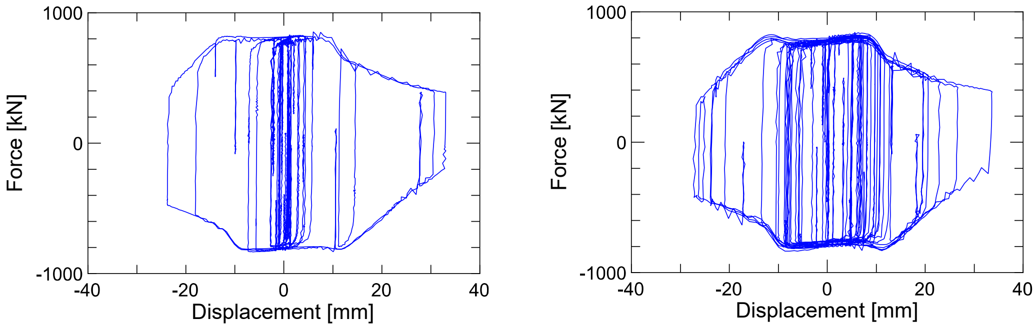

(a) **(b)**

Figure 18 Hysteresis loops of the variable friction damper (VFD) specimen under the earthquake response wave loadings in the full-scale tests[44]: **(a)** run 8; and **(b)** run 9

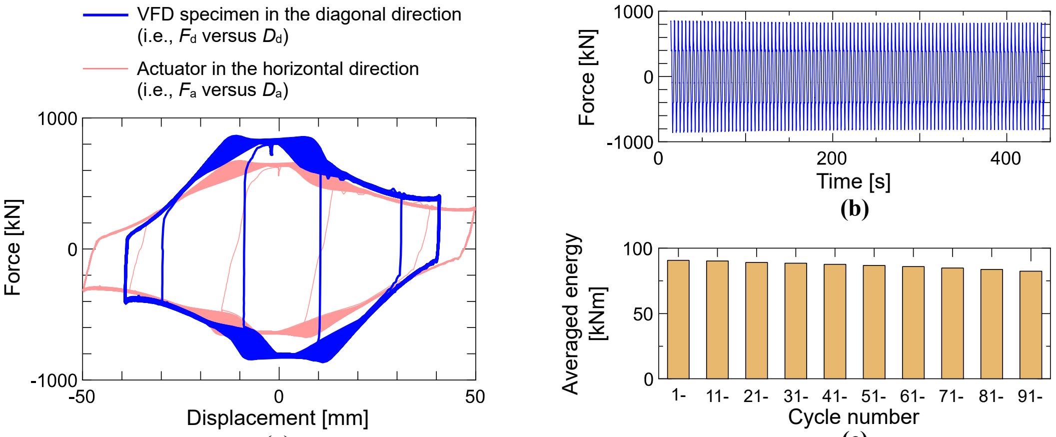

(a) **(c)**

Figure 19 Results of the variable friction damper (VFD) specimen under the 100-cycle loading (run 10) in the full-scale tests: **(a)** hysteresis loops of the VFD specimen and actuator; **(b)** time history damper force[44]; and **(c)** damper hysteretic energy averaged every 10 cycles

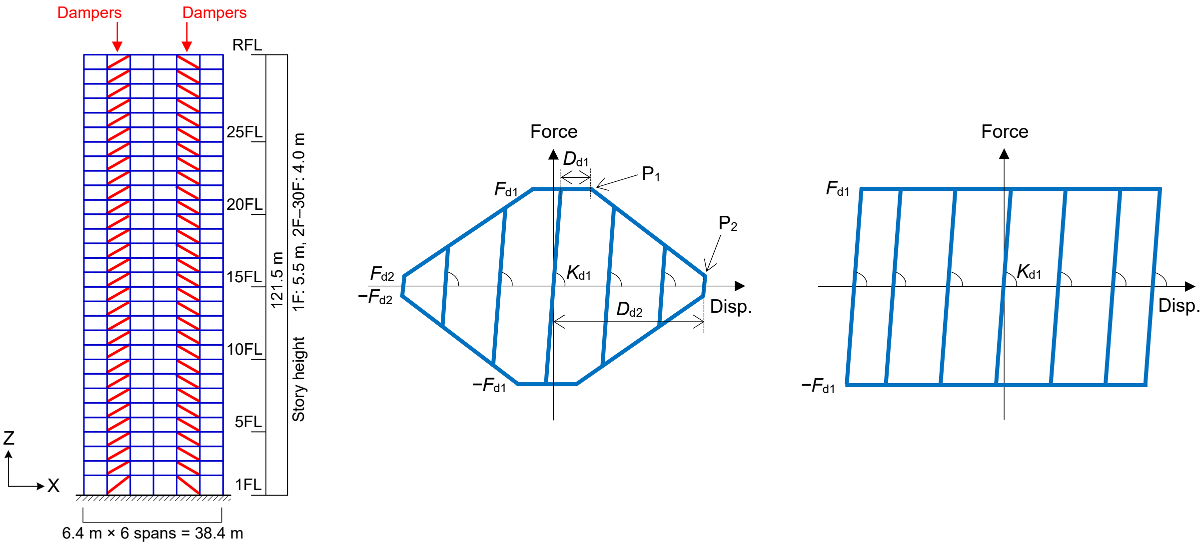

(a) (b) (c)

Figure 20 Numerical two-dimensional (2D) models for the earthquake response analysis: **(a)** elevation view of Models VFD or FD; **(b)** restoring force characteristics of the variable friction damper (VFD) in the damper axis including the brace member in series; and **(c)** restoring force characteristics of the conventional friction damper (FD) in the damper axis including the brace member in series

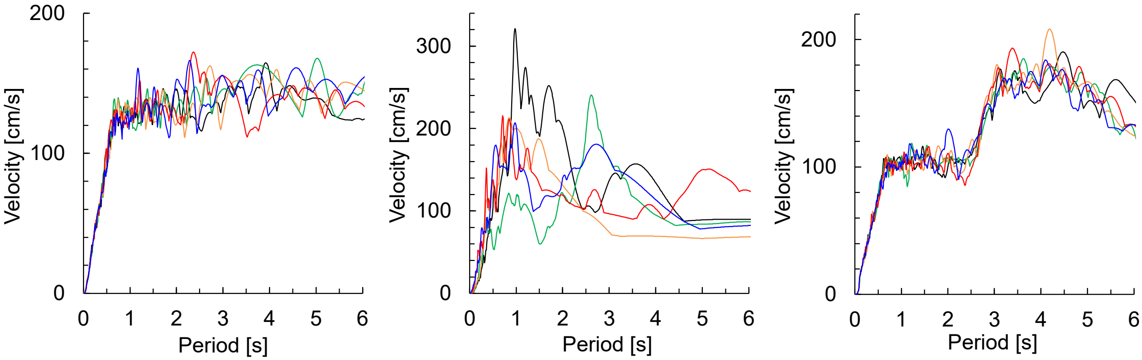

(a) (b) (c)

Figure 21 Velocity response spectra of the input motions (damping factor of 5%): **(a)** simulated waves (M1–M5, input multiplier 1.5); **(b)** observed records (Elcn, Taft, Hach, Tohk, and Kobe; peak ground velocity (PGV) 0.75 m/s); and **(c)** long-period, long-duration (LPLD) ground motions (LPLD1–LPLD5, input multiplier 1.25)

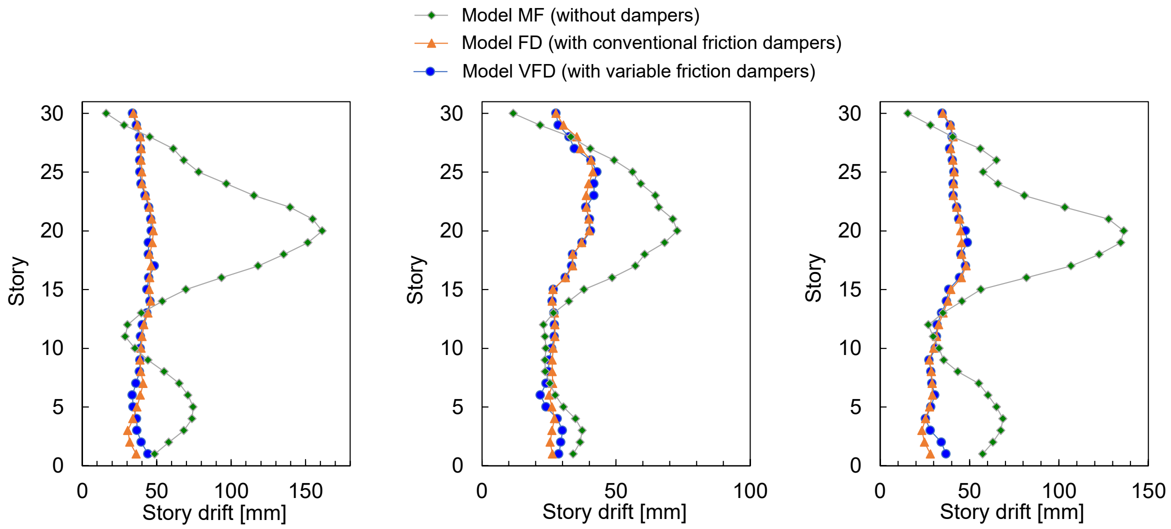

(a) (b) (c)

Figure 22 Peak story drift response (maximum value in each input motion group): **(a)** simulated waves (M1–M5); **(b)** observed records (Elcn, Taft, Hach, Tohk, and Kobe); and **(c)** long-period, long-duration (LPLD) ground motions (LPLD1–LPLD5)

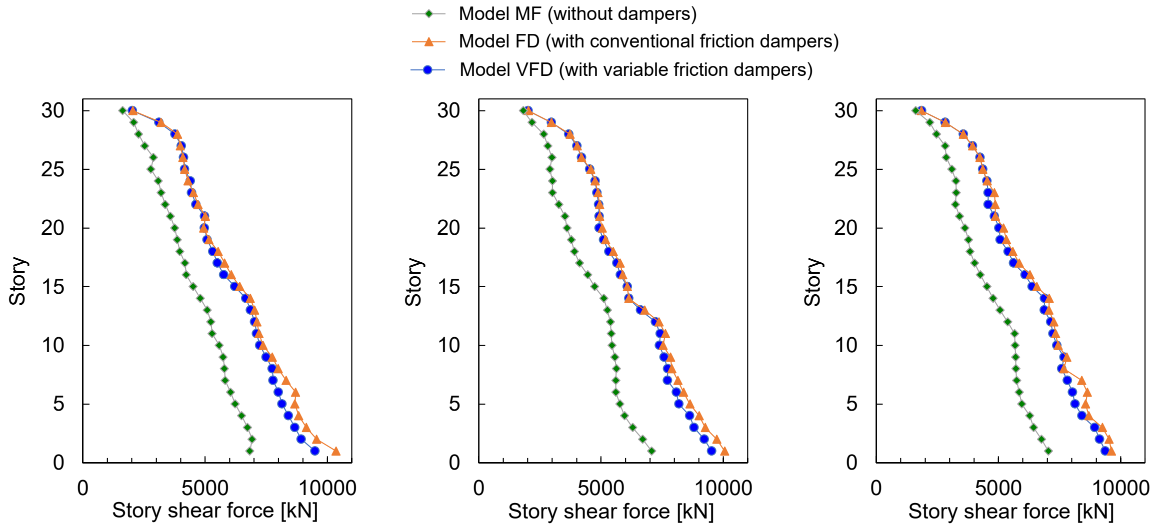

(a) (b) (c)

Figure 23 Peak story shear force response (maximum value in each input motion group): **(a)** simulated waves (M1–M5); **(b)** observed records (Elcn, Taft, Hach, Tohk, and Kobe); and **(c)** long-period, long-duration (LPLD) ground motions (LPLD1–LPLD5)

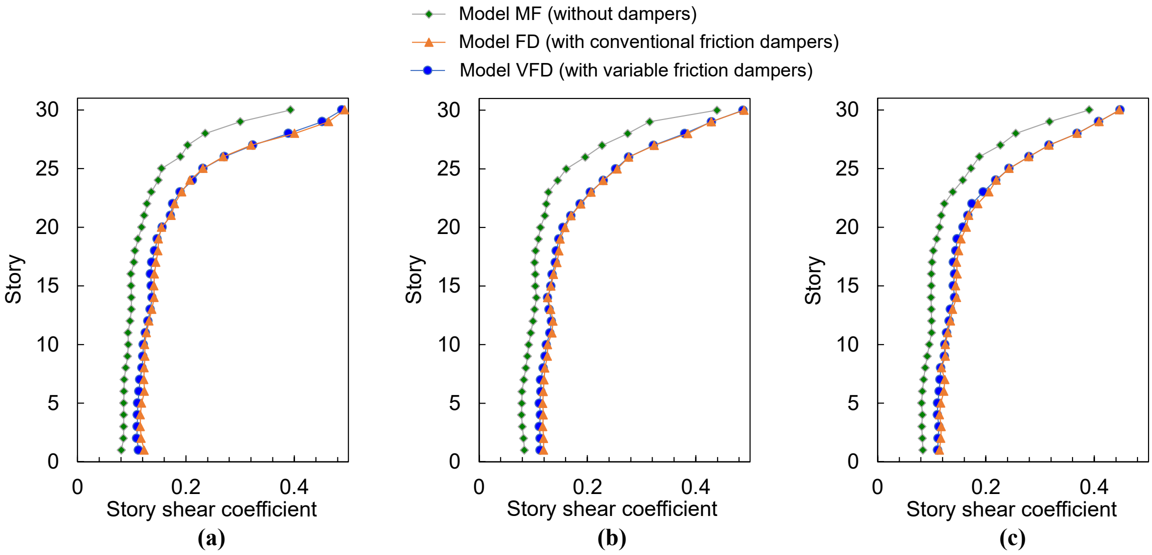

Figure 24 Peak story shear coefficient response (maximum value in each input motion group): **(a)** simulated waves (M1–M5); **(b)** observed records (Elcn, Taft, Hach, Tohk, and Kobe); and **(c)** long-period, long-duration (LPLD) ground motions (LPLD1–LPLD5)

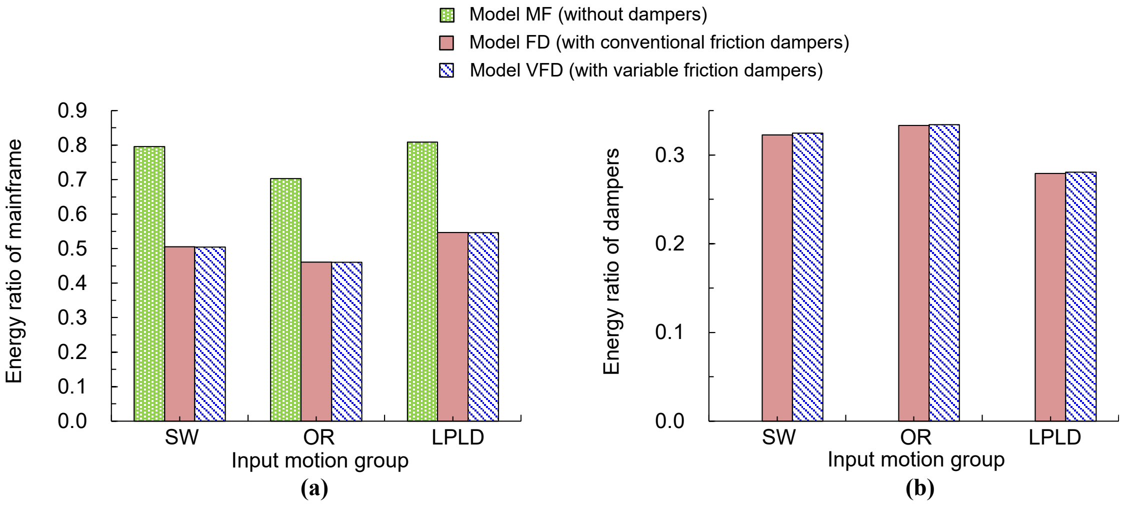

Figure 25 Ratio of the hysteretic energy dissipated by the mainframe and dampers to the total input energy, obtained as the summation of all members in all stories, averaged over each input motion group (SW: simulated waves, OR: observed records, LPLD: long-period, long-duration ground motions): **(a)** energy ratio for the mainframe; and **(b)** energy ratio for the dampers